



HAL
open science

Polypropylene cracking on embryonic and ZSM-5 catalysts – An operando study

Karolina Tarach, Mariame Akouche, Kamila Pyra, Valentin Valtchev, Gabriela Jajko, Jean-Pierre Gilson, Kinga Góra-Marek

► **To cite this version:**

Karolina Tarach, Mariame Akouche, Kamila Pyra, Valentin Valtchev, Gabriela Jajko, et al.. Polypropylene cracking on embryonic and ZSM-5 catalysts – An operando study. *Applied Catalysis B: Environmental*, 2023, 334, pp.122871. 10.1016/j.apcatb.2023.122871 . hal-04270575

HAL Id: hal-04270575

<https://hal.science/hal-04270575v1>

Submitted on 4 Nov 2023

HAL is a multi-disciplinary open access archive for the deposit and dissemination of scientific research documents, whether they are published or not. The documents may come from teaching and research institutions in France or abroad, or from public or private research centers.

L'archive ouverte pluridisciplinaire **HAL**, est destinée au dépôt et à la diffusion de documents scientifiques de niveau recherche, publiés ou non, émanant des établissements d'enseignement et de recherche français ou étrangers, des laboratoires publics ou privés.

28 1 INTRODUCTION

29 A wide variety of plastics meet the requirements of many segments of the economy in a cost-
30 competitive way. Polypropylene (PP) and polyethylene (PE) are the most common type of polyolefins,
31 and their 2022 market size is nearly USD 300 billion with a predicted 5% CAGR (Compound Annual
32 Growth Rate) till 2030 [1]; they account for more than 2/3 of the annual plastics production. One
33 application, consumer product packaging, is in direct daily contact with people, *i.e.*, each of us. A so
34 far inefficient collection of these and all non-biodegradable plastics generates an unsustainable
35 amount of severe pollution, marine plastics being the highly visible tip of this iceberg. Currently, only
36 16 % of plastic waste is reused to make new plastics, with less than 1% chemically reprocessed to
37 provide the original building blocks, *i.e.*, a true circular economy. So, a large proportion of plastics is
38 either left scattered in nature, landfilled, mechanically (down)recycled, or incinerated [1].
39 Depolymerization back to the original monomers is ideally the best approach to chemical recycling and
40 is already taking place for some polyamides and polyesters. It is not yet the case for polyolefins,
41 although they contribute significantly to plastic waste. Their thermal cracking produces a broad range
42 of hydrocarbons requiring further processing to meet the requirements of transportation fuels or
43 higher value (petro)chemicals [2]. Catalysis has a role to play in solving such an important societal
44 challenge. Catalytic cracking, for instance, could bring a combination of higher activity and better
45 selectivity control (narrower product distribution requiring less downstream processing) while working
46 under milder operating conditions (*e.g.*, temperature). All these features indicate potential economic
47 benefits; moreover, catalytic solutions could benefit from the vast experience of existing processes
48 (*e.g.*, FCC [Fluid Catalytic Cracking]), practiced and optimized over at least 70 years on a large scale.
49 Catalytic cracking of polyolefins (polyethylene PE, polypropylene PP) to produce their olefinic
50 monomers has already received attention in previous studies using zeolites [3]. They deserve special
51 attention as their acid sites located in well-defined micropores (~ 0.5-1.0 nm) contribute greatly to the
52 upgrading of heavy oil fractions (atmospheric and vacuum residues) to gasoline (C₅₋₁₁) and/or lower
53 olefins (C₃₋₅) [4]. Polyolefins are intrinsically a less complex feedstock than heavy oil fractions as they
54 are made mostly of C-C and C-H bonds while heavy oil fractions contain significant amounts of S, N,
55 metals (Fe, Ni, V...) spread between many high molecular weight hydrocarbons with high C/H ratios
56 (*e.g.*, polyaromatics) poisoning many catalysts. The downside of zeolites is the presence of severe
57 diffusion limitations resulting in limited use of all their potential "active" sites when bulky molecules
58 are involved. One of the earliest explored remedies is the design of hierarchical zeolites where
59 connected mesopores are added post-synthesis to the pristine micropores, a so-called top-down
60 route. An alternative bottom-up strategy is to synthesize small zeolite crystals, the so-called nano-
61 zeolites [5]. Another promising approach could be based on the so-called embryonic zeolites (EZ) [6,7];

62 these X-Ray amorphous materials, harvested in the early stages of zeolite synthesis, lack the long-range
63 order of zeolites, but their active sites are more accessible enabling the conversion of bulky molecules
64 such as 1,3,5 – triisopropylbenzene (TiPBz, kinetic diameter: 1.1 nm) as their pore size can be
65 engineered in a wider range (1–2.5 nm) [8]. While TiPBz can also be dealkylated on μm -sized ZSM-5,
66 this can only occur on the very few acid sites present on the external surface of the crystals. EZ also
67 possess an advantage over amorphous Silica-Aluminas (ASA) as their tetrahedral Al is more resilient to
68 thermal treatments and therefore keep more of their original acidity due to a reduced dealumination.
69 EZ could therefore extend the range of applications of current zeolites in the processing of polyolefins
70 [9].

71 The present work investigates for the first time the potential use of these acidic X-ray amorphous EZ
72 to deconstruct polypropylene into useful lower molecular weight molecules. They are compared to a
73 purely microporous ZSM-5 and hierarchical zeolites produced by caustic leaching biased towards de-
74 silication [8]. Particular attention is paid to the effect of acid site strength (related to the confined
75 environment) and pore dimensions.

76 **2 EXPERIMENTAL**

77 **2.1 Materials**

78 *EZ-ZSM-5 and H-ZSM-5*

79 The embryonic zeolite was prepared according to the procedure described in ref. 7, using a gel with a
80 Si:Al ratio of 50 and tetrapropylammonium (TPA) as a structure-directing agent. This embryonic zeolite
81 is hereinafter referred to as EZ-ZSM-5. The fully crystalline counterpart of EZ, herein denoted as H-
82 ZSM-5, was obtained from the same initial system after crystallization at 150°C for 2 days.

83 *Hierarchical zeolites*

84 Two hierarchical zeolites are derived from a common ZSM-5 (CBV 28014, Si/Al = 150, Zeolyst
85 International) by leaching it with 0.2 M and 0.5 M NaOH solutions at 65 °C for half an hour [10].
86 Typically, 100 ml of the alkaline solutions are added to 3.0 g of zeolite. After each treatment, the
87 suspension is cooled in an ice-bath and filtered. The resulting hierarchical zeolites are washed with
88 deionized water until neutral pH, ion-exchanged four times with a 0.5 M NH_4NO_3 solution at 60 °C for
89 1 h then filtered, washed, and dried at room temperature. The two resulting materials are referred to
90 as deSi-0.2-ZSM-5 and deSi-0.5-ZSM-5, where x in deSi-x-ZSM-5 indicates the NaOH concentration in
91 solution; deSi reminds us that during such an hierarchization, Si is preferentially extracted from the
92 zeolite framework.

93 2.2 Characterization

94 The chemical composition of the catalysts is determined by inductively coupled plasma optical
95 emission spectrometry (ICP-OES, Optima 2100DV, PerkinElmer).

96 The powder X-ray diffractions are recorded on a Rigaku Multiflex diffractometer using the Cu K α
97 radiation (40 kV, 40 mA).

98 Transmission Electron Microscopy (TEM) of the materials is done on a JEOL-2011F with an acceleration
99 voltage of 200 kV. Prior to characterization, all samples are dispersed in isopropanol and ultrasonicated
100 for 30 min and then dropped onto a carbon film on a copper grid.

101 The porosity is measured by nitrogen adsorption/desorption isotherms on a Quantachrome
102 Autosorb-1-MP volumetric analyser. All samples are degassed under 10^{-5} mbar at 350 °C for 24 h
103 before measurement. The specific surface area, S_{BET} , is calculated using the Brunauer-Emmett-Teller
104 method, and the total pore volume (V_{total}) is taken from the nitrogen volume adsorbed at $p/p_0 = 0.985$.
105 The micropore volume (V_{micro}) is calculated using the t -plot method and the mesopore volume (V_{meso})
106 is BJH adsorption cumulative volume of pores between 1.7 – 30 nm diameter. By analogy, the S_{meso} is
107 BJH adsorption cumulative surface area.

108 The acidic features of the catalysts are assessed by IR monitoring of adsorbed probes (CO and Pyridine).
109 All IR spectra are recorded with a resolution of 2 cm^{-1} on a Bruker Invenio X FTIR spectrometer fitted
110 with an MCT detector in the range 4000–400 cm^{-1} . The samples are pressed into self-supported wafers
111 (10 mg per 1cm^2), placed in an IR cell connected to a vacuum line, activated under vacuum (10^{-6} torr)
112 at 500 °C for 1 h and then cooled down to acquire the spectra at room temperature.

113 CO (Linde Gas Poland, 99.95%) is adsorbed at –140 °C up to saturation of the Lewis acidic sites (bands
114 at 2230, 2225 cm^{-1} and 2190 cm^{-1}) and the appearance of hydrogen-bonded CO to Brønsted Si(OH)Al
115 sites (band at 2175 cm^{-1}).

116 Pyridine (Py) (Avantor) is adsorbed at 170 °C. Each sample is saturated with Py and the cell evacuated
117 at 170 °C to remove gaseous and physisorbed Py. The Brønsted (BAS) and Lewis (LAS) acid sites
118 concentration are obtained from the integrated area of the adsorbed pyridine bands at 1560–1535
119 (pyridinium ions, PyH^+) and 1440–1460 cm^{-1} (Py-Lewis site adduct) by using extinction coefficients
120 reported earlier [11]. The acid strength is assessed by Py thermodesorption, where all samples are
121 heated to 350 °C, kept there for 10 min, cooled to 170 °C where IR spectra are recorded. The ratio
122 between Py adsorbed at 350 °C and 170 °C describes the acid strength of the various catalysts.

123 The Brønsted acid sites located on the external and mesoporous surfaces of ZSM-5 are quantified by
124 IR monitoring of the adsorption at 200 °C of 2,6-di-tert-butylpyridine (di-TBPy, Sigma–Aldrich, >97 %,
125 kinetic diameter: 0.8 nm), desorption under vacuum at 200°C (15 min) and cooling down to room
126 temperature. The 1615 cm⁻¹ band intensities of di-TBPyH⁺ (molar extension coefficient 0.50
127 cm²·μmol⁻¹) are used to quantify the number of di-TBPy-accessible acid sites [12]. The intensity of di-
128 TBPyH⁺ band is calculated from the spectra recorded after di-TBPy adsorption at 200 °C for 15 min,
129 subsequently cooled down to room temperature. All spectra are normalized to a 10 mg weight.

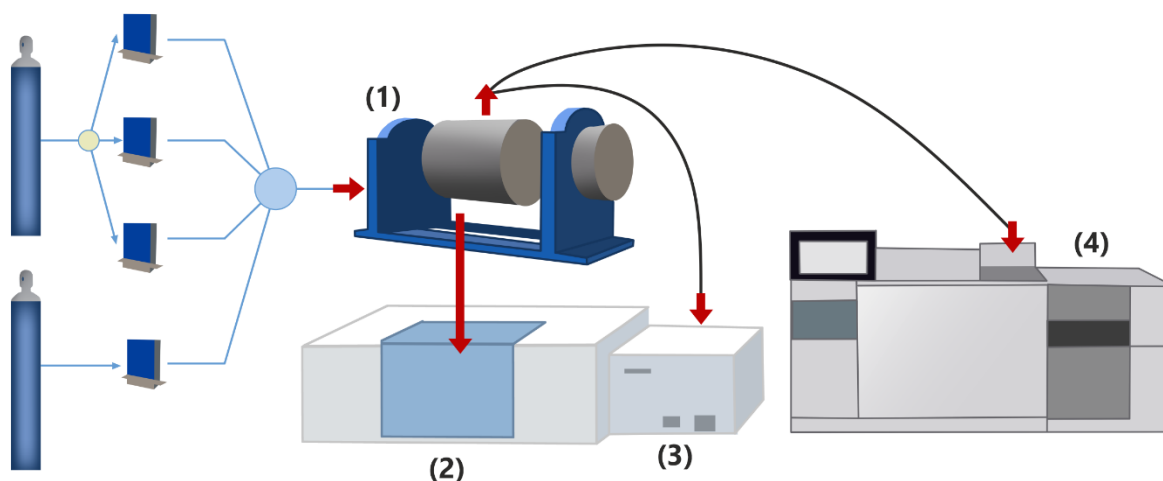
130 **2.3 Catalytic cracking of polypropylene**

131 Low density polypropylene, PP, (Alfa Aesar, Product No.: 42607, Lot No.: P28D047) is crushed, sieved
132 and the ≤250 microns fraction retained for testing. The catalytic cracking of PP takes place in a
133 thermobalance (TGA/SDTA Mettler Toledo). 10 mg of zeolite powder is mixed for 10 min with PP (30
134 mg) in an agate mortar, 10 mg are transferred to an α-Al₂O₃ crucible in the thermobalance. The
135 polymer cracking takes place within the 30 °C - 600 °C temperature range under a heating rate of 5
136 °C/min under N₂ flow (80 mL·min⁻¹). The catalyst weight and adsorbed moisture are considered to
137 calculate the degree of conversion and level of coke left on the catalysts. After the reaction, all samples
138 are cooled to 30 °C and then flushed with dry synthetic air (80 mL·min⁻¹). The coke content is the mass
139 change after heating to 800 °C at a rate 30 °C·min⁻¹. For comparative purposes, pure PP is cracked
140 thermally, *i.e.*, without any catalyst. The TGA was connected with GC-MS setup to follow the eluted
141 products.

142 **2.4 FT-IR & GC&MS *operando***

143 An *operando* setup is used to study the PP degradation. A self-supporting disc (ca. 5.5-6 mg·cm⁻²) of
144 the catalyst and PP in 1:1 ratio is placed in a 2 cm³-volume quartz IR cell (MeasLine,
145 www.measline.com, patent PL232633, Poland). The homogeneity of the zeolite/catalyst mixtures is
146 identical to the TGA setup and the room temperature IR spectra are normalized to the same intensity
147 of the overtone bands (2050–1800 cm⁻¹). As in each spectrum, the intensity of the 2960 cm⁻¹ (–CH₃)
148 and 2925 cm⁻¹ (–CH₂) bands are similar, an equal amount of catalyst can be assumed. During the
149 reaction, the catalyst surface as well as the gas phase are monitored simultaneously, Figure 1. N₂, the
150 carrier gas (flowrate = 30 ml/min, 110°C) is introduced along Teflon lines (1/16'') and the *operando* IR
151 cell with the catalyst/PP wafer heated from room temperature to 250 °C (ramp of 10 °C·s⁻¹) till full
152 polymer conversion. Time-resolved spectra are collected on the FT-IR spectrometer and the products
153 simultaneously analysed by mass spectrometry (MeasLine, www.measline.com, RGA200) and gas
154 chromatography (Agilent Technologies 7890B). Coke and tars are included to compute catalyst
155 selectivity.

Operando FT-IR/GC-MS mode



156

157 **Figure 1.** Operando IR cell fed by independently controlled flowing gases (1), coupled to four detectors: IR
158 spectrometer (2), IR gas cell (3), GC-MS (4).

159 2.5 2D COS analysis of FT-IR spectroscopy results

160 Due to the complexity of the polymer cracking, a two-dimensional correlation analysis (2D COS IR) is
161 helpful to monitor both the PP cracking and the subsequent coke combustion on a catalytically active
162 surface. 2D maps with contour plots along two axes (wavenumbers and correlation intensity) enable
163 better monitoring of the reaction as a function of time on stream than conventional 1D spectra with
164 numerous overlapping bands. Typically, a synchronous 2D correlation map highlights simultaneous or
165 coincident events identified by two separate bands (ν_1 and ν_2) upon an externally triggered
166 perturbation, a chemical reaction in this case. A positive ν_1 - ν_2 correlation indicates a simultaneous
167 increase or decrease in the intensity of these bands, while a negative correlation indicates that the
168 intensity of one band (*e.g.*, ν_1) changes at the expense of the other (*e.g.*, ν_2).

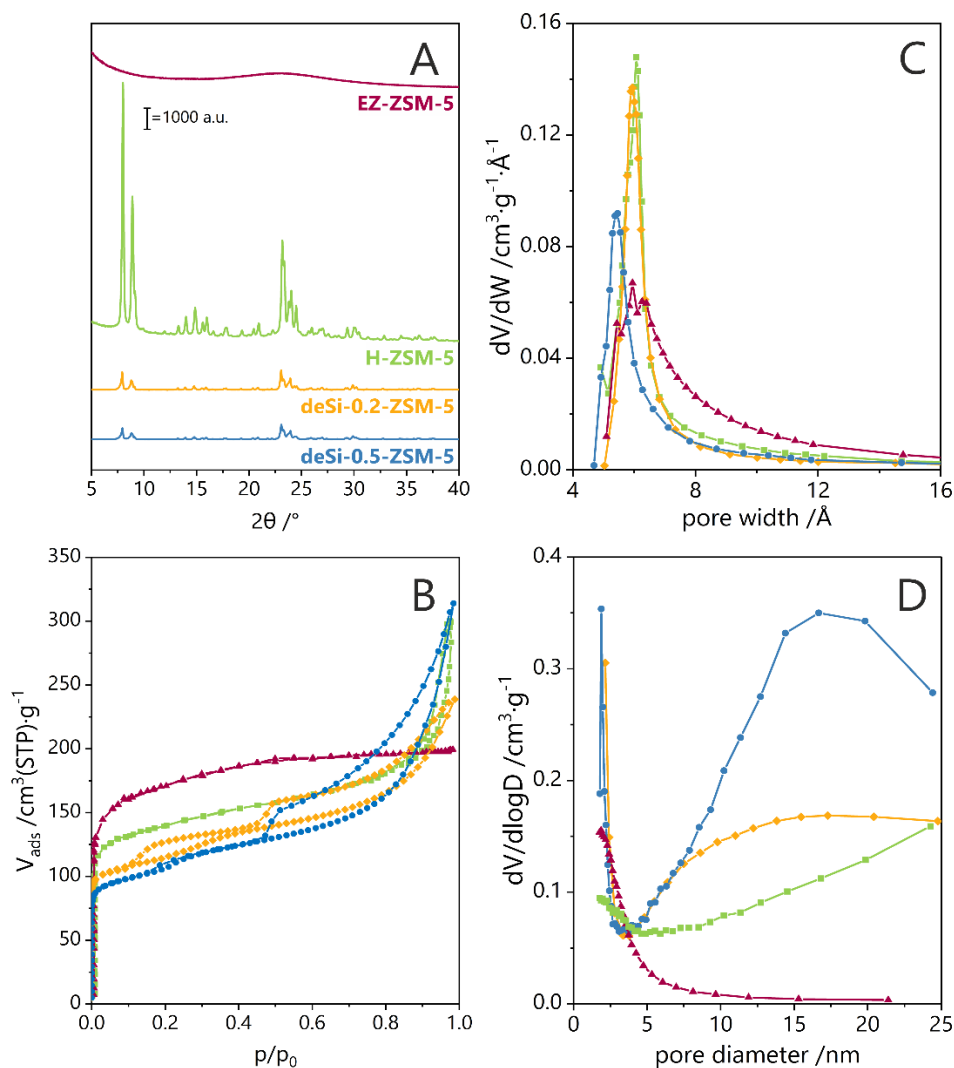
169

170 3 RESULTS AND DISCUSSION

171 3.1 Characterization of the catalysts: structure, texture & acidity

172 The catalysts used in PP cracking possess similar or different structural, textural, and acidic properties
173 to better assign their performances to specific features. Figure 2A highlights that EZ-ZSM-5 with a bulk
174 Si/Al ratio of 50 is X-ray amorphous while the purely microporous H-ZSM-5 and hierarchical samples
175 (deSi-0.2-ZSM-5 and deSi-0.5-ZSM-5) all display the MFI-type structure. The deSi-0.5-ZSM-5
176 hierarchical zeolite and EZ-ZSM-5 have close Si/Al while deSi-0.2-ZSM-5 is less desilicated. The H-ZSM-
177 5 exhibits a type I N_2 adsorption isotherm with a steep nitrogen uptake at low relative pressure,
178 indicating the presence of micropores ($< \sim 1$ nm) (Fig. 2 B). Textural mesopores are evidenced by a

179 second uptake at higher relative pressures. EZ-ZSM-5 displays a type I(b) N₂ adsorption isotherm
 180 characteristic of larger micropores and/or smaller mesopores (< ~ 2.5 nm) [13]. The micropores in H-
 181 ZSM-5 and hierarchical zeolites are, as expected, in the 0.50-0.60 nm range. EZ-ZSM-5 has
 182 supermicropores (> 0.7 nm), as well as ultra-microporosity (Fig. 2C). The two hierarchical catalysts,
 183 deSi-0.5-ZSM-5 and deSi-0.2-ZSM-5, display type IV isotherms with mixed H2 and H4 hysteresis loops
 184 [14] in the P/P° range 0.5–0.9 indicative of intracrystalline bottlenecked mesopores and mesopores
 185 connected to the outer surface. Mesoporosity is more important in the two deSi-x-ZSM-5 and centred
 186 around 18 nm (Fig. 2D). No mesoporous characteristic is visible for EZ-ZSM-5. The indexed hierarchy
 187 factor (IHF, see Table 1) is helpful as it measures the alteration of textural properties [10], *i.e.* higher
 188 IHF indicates a greater share of mesopores while microporosity is preserved and lower IHF witness
 189 either an excess in microporosity or mesoporosity. In our case, a high hierarchization degree with
 190 preserved microporosity occurs only for deSi-0.5-ZSM-5 (IHF = 0.50).



191
 192 **Figure 2.** A) XRD powder patterns. B) N₂ adsorption–desorption isotherms. C) Micropore size distributions. D) BJH
 193 pore size distributions.

194
195

Table 1. Chemical composition (ICP) and textural properties (N_2 physisorption) data.

Sample	Si/Al ^a	V_{total} cm^3g^{-1}	V_{micro}^b cm^3g^{-1}	V_{meso}^c cm^3g^{-1}	S_{BET} m^2g^{-1}	S_{micro} m^2g^{-1}	S_{meso} m^2g^{-1}	IHF ^d
EZ-ZSM-5	50	0.30	0.26	0.05	601	575	78	0.34
H-ZSM-5	65	0.62	0.19	0.11	535	447	78	0.25
deSi-0.2-ZSM-5	124	0.40	0.15	0.15	433	335	98	0.25
deSi-0.5-ZSM-5	48	0.49	0.13	0.34	393	278	156	0.36

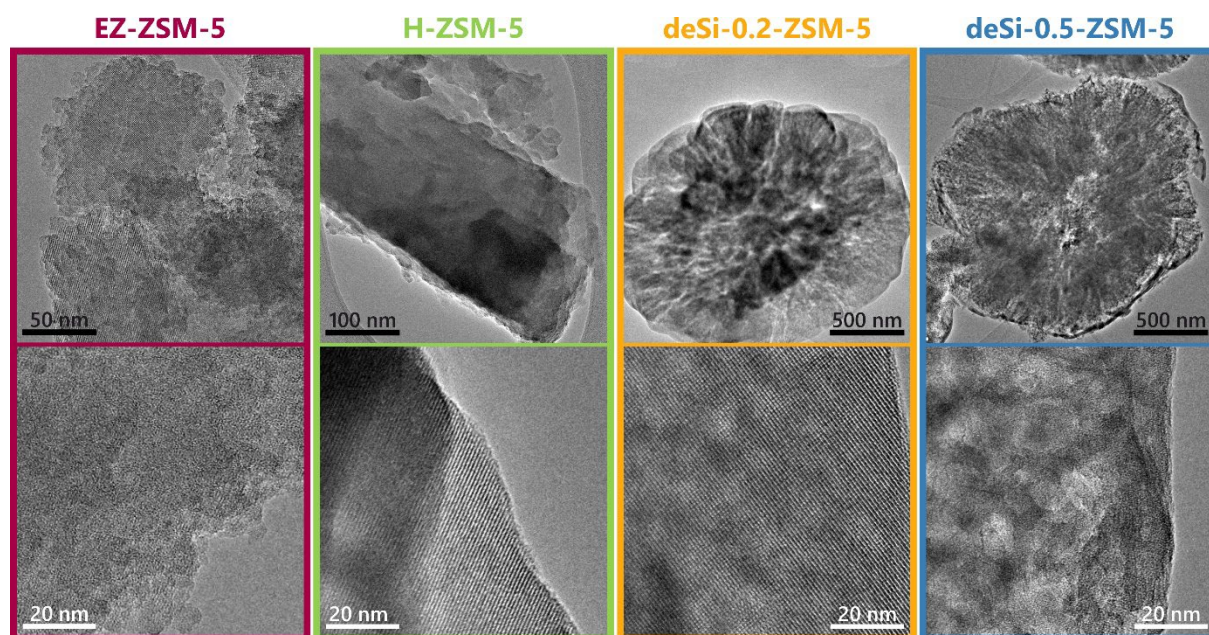
196 *a*: ICP

197 *b*: t-plot method with thickness between 4 and 9.2Å, P/P^* (0.05, 0.8)

198 *c*: DFT

199 *d*: IHF (index hierarchy factor) calculated as $(V_{micro}/V_{micro,max}) \times (S_{meso}/S_{meso,max})$ [10].

200 TEM micrographs are gathered in Figure 3. H-ZSM-5 consists of 400 nm aggregates, while EZ-ZSM-5
201 shows *ca.* 3-8 nm featureless aggregates. The mildly desilicated deSi-0.2-ZSM-5 shows uniform
202 mesopores from the external surface to the interior of the zeolite microporosity. The more severely
203 leached deSi-0.5-ZSM-5 consists of core-shell particles with macropores on its external shell and
204 zeolite mesoporosity elsewhere. The presence of Al-rich external layer can be anticipated from dense
205 shell displayed in deSi-0.5-ZSM-5. These features are consistent with N_2 physisorption indicating the
206 presence of macro- and meso-porosity in deSi-0.5-ZSM-5.

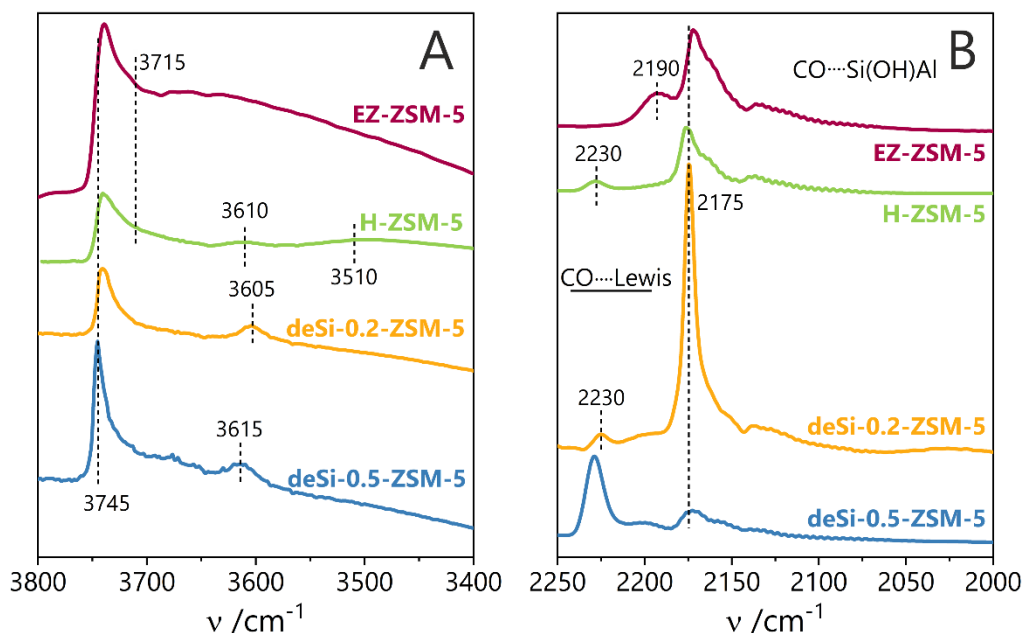


207

208 **Figure 3.** Transmission electron microscopy images.

209 Figure 4A shows the IR spectra of silanols and bridged hydroxyls on all catalysts. EZ-ZSM-5 stands out
210 with the highest population of isolated $(SiO)_3Si-OH$ (3756 cm^{-1}) and internal (3715 cm^{-1}) silanols
211 together with many hydrogen-bonded silanols (broad band around 3510 cm^{-1}). As expected, the silanol
212 population in the two desilicated zeolites is higher than their parent and the increased intensity of
213 isolated Si-OH follows the increasing mesoporous area of deSi-0.5-ZSM-5 and deSi-0.2-ZSM-5 [15]. The
214 bridging hydroxyls, $Si(OH)Al$, located between $3615\text{--}3605\text{ cm}^{-1}$ on the three crystalline zeolites are
215 absent on EZ-ZSM-5, a common feature on amorphous aluminosilicates where a wider spread of T-O-

216 T angle leads to negligible intensities of the corresponding Si(OH)Al bands [16]. A more precise analysis
 217 of the surface acidity is worth exploring as silanols can sometimes display acidity in the range of
 218 bridged hydroxyls and therefore promote hydrocarbon transformation as cracking and coking [17].



219
 220 **Figure 4.** IR spectra: (A) pristine O-H groups (25 °C) and (B) CO adsorbed on acid sites (-100 °C).

221 **Table 2.** Acidity parameters of the catalysts.

Sample	Si/Al	C_{BAS}^a $\mu\text{mol g}^{-1}$	C_{LAS}^a $\mu\text{mol g}^{-1}$	$C_{BAS} + C_{LAS}^a$ $\mu\text{mol g}^{-1}$	AF_{BAS}^b %	ν_{OH}^c cm^{-1}	BAS^d A_{350}/A_{170}	LAS^d A_{350}/A_{170}
EZ-ZSM-5	50	40	30	70	69	-	0.25	0.30
H-ZSM-5	65	115	25	140	3	3610	0.42	0.80
deSi-0.2-ZSM-5	124	95	32	127	50	3605	0.61	0.65
deSi-0.5-ZSM-5	48	140	140	280	33	3615	0.15	0.75

222 *a*: Brønsted (C_{BAS}) and Lewis (C_{LAS}) sites concentration determined by FTIR (Py adsorption)

223 *b*: Brønsted acid sites accessibility factor (AF_{BAS}), i.e., % of acid sites accessible to di-TBPy vs. C_{BAS} accessible to Py

224 *c*: strength of the acidic Si(OH)Al measured by the band shift upon hydrogen bonding with CO at -100 °C (spectra not shown)

225 *d*: Brønsted and Lewis sites strength (A_{350}/A_{170}) determined by FTIR (Py adsorption)

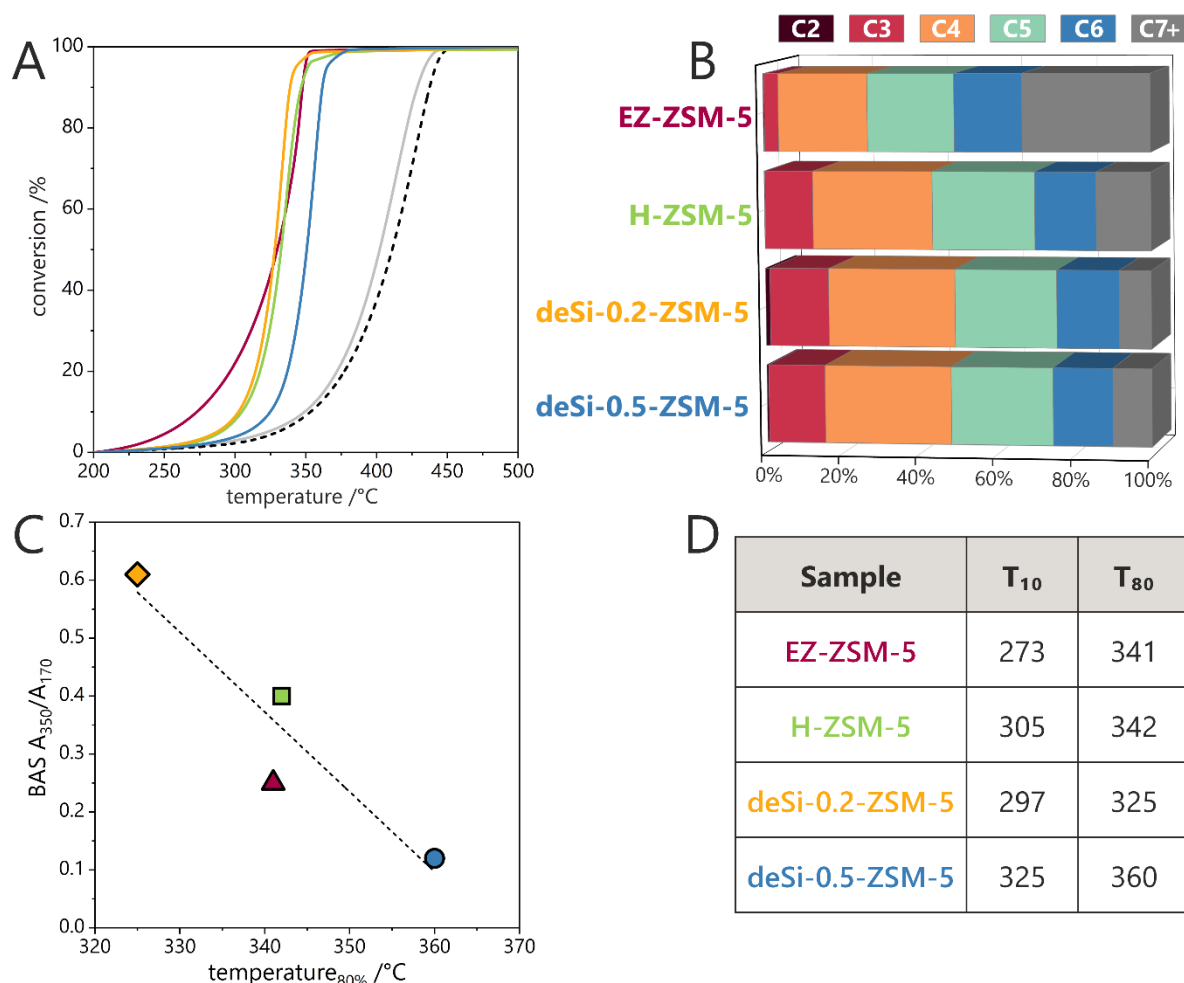
226
 227 Acid site concentration and strength is measured by FTIR monitoring of Py adsorption (Table 2). The
 228 EZ-ZSM-5 and highly mesoporous deSi-0.5-ZSM-5 possess the highest number of LAS, namely 43-50%
 229 of the total acidity. The origin of this important Lewis acidity on the embryonic and hierarchical zeolites
 230 is further examined by CO adsorption monitored by FT-IR (Fig. 4B). The CO spectra on EZ-ZSM-5 shows
 231 a band at 2190 cm^{-1} indicative of its interaction with minor fraction of LAS of weak and/or moderate
 232 strength, i.e., extra-framework aluminium species (EFAL species). We showed earlier that after
 233 calcination (refs 6, 7), only a minor quantity of Al is octahedrally coordinated, in contrast to what
 234 happens to conventional ASA's (amorphous silica alumina's) [18]. On deSi-0.5-ZSM-5, bands at 2225-
 235 2220 cm^{-1} witness the presence of coordinatively unsaturated of alumina clusters (EFAL species, LAS)
 236 with high strength formed after dehydroxylation of two neighbouring Si(OH)Al species [19,20]. On H-

237 ZSM-5 and deSi-0.2-ZSM-5, both with lower mesoporosity, Brønsted acidity is prevalent as the relative
238 share of LAS does not exceed 25% (Table 2); they could affect accessibility to the microporous acidity.
239 2,6-di-tert-butylpyridine (di-TBPy) adsorption monitored by FTIR, widely used to measure the Brønsted
240 acidity of the external/mesoporous surface of zeolites [12,21] is reported in Table 2 with the
241 Accessibility Factor (AF_{BAS} = percentage of BAS concentration measured by di-TBPy vs. Py adsorption).
242 As expected, on H-ZSM-5 very few BAS are located on its external surface (AF_{BAS} = 3%) while on deSi-
243 0.2-ZSM-5 (high intracrystalline mesoporosity) and EZ-ZSM-5 (high intercrystalline mesoporosity) at
244 least half of the BAS protonate di-TBPy (AF_{BAS} = 50-69%). DeSi-0.5-ZSM-5, with the highest IHF (Table
245 1) has the lowest AF_{BAS} of the 3 mesoporous catalysts. Realumination followed by dehydroxylation is
246 the most common explanation of the alteration of acid sites in alkaline leached zeolites [10,19]. The
247 high concentration of LAS on deSi-0.5-ZSM-5 is responsible for micropores clogging and limited
248 accessibility of its BAS.

249 Acid strength is another parameter to consider in zeolitic catalysts. Pyridine thermal desorption, TPD,
250 (A_{350}/A_{170} , Table 2) indicates a potentially higher acid strength of the BAS in H-ZSM-5. The introduction
251 of mesoporosity in ZSM-5 zeolites reduces the apparent acid strength of protonic sites; they appear
252 “weaker” due to differences in confinement between meso- and micropores [22]. The strength of
253 protonic site can also be influenced by close proximity with extraframework Al and silanols [9,23]. The
254 defect-rich EZ-ZSM-5 follows this rule as a lower protonic acid strength appears. The desilicated
255 zeolites can be also considered less perfect with partially extracted Al near framework atoms. It is the
256 case of deSi-0.5-ZSM-5 with a BAS strength similar to EZ-ZSM-5 while deSi-0.2-ZSM-5 possesses the
257 highest protonic strength due to its higher Si/Al as often reported [24,25]. These trends are also
258 aligned with the stretching frequencies of the Si(OH)Al (ν_{OH} , Table 2, Fig. 4A), *i.e.*, the lower ν_{OH} , the
259 longer O-H bond, thus higher the acidity of the corresponding proton. As usual, TPD of basic molecules
260 on hierarchical zeolites should be taken with some caution as differences in diffusion pathlengths could
261 affect diffusion/adsorption ratios of the probe and therefore the maximum temperature in the TPD
262 profile of the basic probe [26].

263 **3.2 Polypropylene cracking: thermogravimetry and *operando* FT-IR-GC-MS**

264 The effects of the different textural and acidic properties of the above “ZSM-5 catalysts” are tested in
265 the catalytic cracking of PP (polypropylene). Figure 5A highlights PP conversion (weight loss measured
266 in a thermobalance) as a function of temperature in a typical “Light-off” diagram, along with the
267 thermal cracking of pure PP as a reference. T_{10} and T_{80} (temperature for 10% and 80 % conversion, Fig.
268 5D) are used as descriptors. The selectivities of the catalysts are measured in an *operando* FT-IR cell
269 fitted with a GC-MS detector (Fig. 5B).



270

271

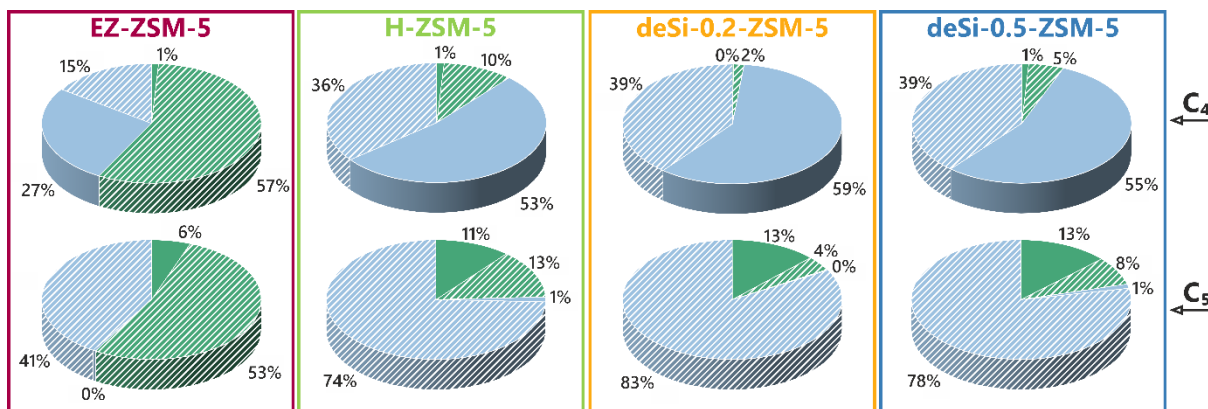
272 **Figure 5.** (A) PP cracking (light-off diagrams) on EZ-ZSM-5, H-ZSM-5 and its two hierarchical zeolites (deSi-0.2-
 273 ZSM-5 and deSi-0.5-ZSM-5, an "inert" SiO₂ (grey) and thermal cracking (dotted curve). (B) Product distribution
 274 from the catalytic PP cracking. (C) T₈₀ variation with BAS (A_{350}/A_{170} ratio). (D) Temperature for 10% and 80 %
 275 conversion, T₁₀ and T₈₀, respectively.

276 In the low-temperature range, EZ-ZSM-5 is the most active catalyst, although it has the lowest
 277 concentration of acid sites highlighting their higher accessibility coupled with a faster diffusion of
 278 reactants and products. Moreover, it cannot be excluded that a portion of the non-bridging silanols
 279 could participate in the reaction as their acidity may not be negligible [27]. Indeed, internal H-bonded
 280 silanols were already found to be more active and selective compared to external silanols in the
 281 Beckmann rearrangement [28]. The EZ sample exhibits the most intense bands at the region typical of
 282 hydrogen bonded silanols (3670 – 3100 cm⁻¹), the involvement of the medium and high acidity silanols
 283 in cracking process should not be neglected. In line with above, the highest contribution of non-acidic
 284 isolated Si-OH (3745 cm⁻¹) in deSi-0.5-ZSM-5 does not offer the significant advancement. [29,30]

285 The presence of an Al-rich layer with many Lewis acid sites in deSi-0.5-ZSM-5, Figures 3 and 4, hampers
286 the diffusion of reactants to the micropores. On deSi-0.2-ZSM-5, with a moderately developed
287 mesopore surface area and low BAS density, the conversion above 350 °C is higher than for other
288 catalysts. A similar critical role of LAS was previously reported by Tarach et al. [19]; a mild
289 dealumination and redistribution of Al on the mesopore surface produces a more open hierarchical
290 porosity. As a result, micropore mouths, free of LAS residues increase BAS accessibility as well as
291 polymer cracking. Verboekend et al. [31] also reported inhibition of LDPE cracking on desilicated ITQ-
292 4 at low conversion (10%) due to the presence of excessive amounts of Lewis acid sites.

293 At about 320 °C, PP conversion on EZ-ZSM-5 increases slower than on H-ZSM-5, indicating that BAS
294 accessibility is not the only factor influencing catalyst performance. The linear dependence of T_{80} PP
295 cracking and BAS strength (A_{350}/A_{170}) of crystalline zeolites highlights the influence of acidic strength
296 on cracking activity at higher temperature range. On EZ-ZSM-5, the reduced acidic strength due to
297 lower confinement is not compensated by a higher BAS accessibility. For instance, in *n*-decane cracking
298 on zeolite Beta, BAS strength is the key factor determining catalytic activity [22]. In LDPE cracking, the
299 porosity of hierarchical Beta zeolites helps when their BAS strength is above 80% of their pristine
300 parent [32,33]. Figs 5 C and D therefore highlight that at low temperature, i.e. at low conversions,
301 where the feedstock is mainly composed of very bulky molecules, active site accessibility is critical
302 while at higher temperatures where reactants are less bulky molecules, “apparent acid strength” will
303 play an increasing role.

304 The quantitative analysis of the PP cracking products by GC-MS shows that on the EZ-ZSM-5 catalyst
305 less C_3 - C_4 (gas) and C_5 - C_6 (liquid), but more C_{7+} are produced compared to H-ZSM-5 and the two
306 hierarchical deSi-*x*-ZSM-5. It is therefore expected that a catalyst with a higher but less confined
307 microporosity populated with BAS with lower strength will not favor secondary cracking. Moreover,
308 on EZ-ZSM-5 more bimolecular reactions are expected due to the closer proximity of bulky reactants
309 in larger cavities [34]. These observations are in line with literature reports [34,35] on the applicability
310 of medium and wide pore zeolites in the catalytic degradation of polyethylene and polypropylene. The
311 influence of the micropore volume, also impacts the side and sequential reactions and will appear later
312 (Fig. 7).



313

314 **Figure 6.** Cracking products distribution in C₄ and C₅ fractions: paraffinic (green), olefinic (blue), branched
 315 (hatched), and linear (filled).

316 The C₄₋₅ product distribution highlights how the structural/textural and acidic properties influence PP
 317 cracking selectivity (Fig. 6). The hydrogen-transfer (HT) ability of zeolites is known to increase with
 318 micropore voids size and BAS density, in turn influencing the paraffin/olefin (p/o) ratio of the products
 319 [36,37]. DeSi-0.2-ZSM-5 and deSi-0.5-ZSM-5 zeolites display a lower HT and therefore produce more
 320 olefins in PP cracking. The large external surface and better acid sites accessibility in hierarchical
 321 catalysts limit the extent of secondary HT reactions as those are favoured by long reactions paths. This
 322 is the case for deSi-0.2-ZSM-5 producing the highest level of olefins. However, for deSi-0.5-ZSM-5,
 323 despite more macro- and meso-porosities, its higher BAS and LAS density promotes HT [38], therefore
 324 producing more paraffins. Moreover, LAS are also reported to interact with BAS to increase the acid
 325 strength of the latter (Table 2) [39,40].

326 EZ-ZSM-5 also increases isomerization (C₄ and C₅ fractions) following a bimolecular mechanism (HT
 327 reactions) in the more spacious voids of its partially formed unit cells. The high silanols population,
 328 which could possess some non-negligible acidity, *vide supra*, can also favor high *iso*-paraffin
 329 production. The inhibition of isomerization (an HT reaction) by shortening the reaction pathlength
 330 upon secondary intercrystalline or intracrystalline mesoporosity addition is observed on H-ZSM-5 and
 331 hierarchical samples. Corma et al. [41] reported that the Si/Al ratio determines the extent of
 332 bimolecular reactions by regulating carbenium ion residence times on the surface. The higher
 333 production of *iso*-C₄ and *iso*-C₅ paraffins in EZ-ZSM-5 could be ascribed to such a feature. Another
 334 source for higher p/o ratio is dehydrogenation reactions to aromatics all the way to coke [42], as the
 335 hydrogen produced can saturate olefins, albeit to a minor extent, as little hydrogen is available from
 336 such a route [38].

337 In PP cracking, EZ-ZSM-5 behaves more like a FAU than an MFI structure. In addition, some EZ-ZSM-5
 338 acidic silanols could also play a role as already reported in zeolites for C₈-olefins and polypropylene

339 [37]. The hierarchical deSi-0.2-ZSM-5 behaves as a zeolite with high acid strength, low acid site density,
340 and microporous confinement leading to low initial conversions (low T) and limited HT. This results in
341 lower p/o ratio and limited coke formation.

342 **3.3 Polypropylene cracking and catalyst coking: 2D COS *operando* FT-IR spectroscopy**

343 The above results are classically produced by relating catalyst characterization to their performances
344 without inspecting the catalyst surface during the reaction. An *operando* study allows to go further
345 and closer to the catalyst surface while in action under realistic conditions of temperature and
346 pressure. The 2D-COS IR technique is particularly suited as it correlates events taking place on the
347 catalyst surface by looking simultaneously at active sites on the catalyst and reactants/products.

348 Time-resolved FT-IR, already proven helpful in hydrocarbon transformations [43,44] is applied here to
349 monitor simultaneously PP cracking and the catalyst surface (Fig. 7). By following the $A_{\nu}(-CH_3)/A_{\nu}(-CH_2)$
350 PP ratio evolution during reaction, where $A_{\nu}(-CH_3)$ and $A_{\nu}(-CH_2)$ represent the intensities of the
351 of $-CH_3$ (2960 cm^{-1}) and $-CH_2-$ (2925 cm^{-1}) bands characteristic for the surface adsorbed species, the
352 influence of the different catalysts is evidenced. The CH_2/CH_3 intensity ratio is widely used to estimate
353 the length and degree of branching of the aliphatic side-chains; the larger this ratio, the longer the
354 aliphatic chain [45–47]. EZ-ZSM-5 is the most active in end-chain cracking at the earliest stages of the
355 reaction (0-3 min), goes through a maximum before decreasing rapidly due to the formation and
356 retention of heavy by-products (coke precursors), leading to deactivation. Such a deactivation step is
357 not observed on deSi-0.2-ZSM-5 where the $A_{\nu}(-CH_3)/A_{\nu}(-CH_2)$ ratio decrease is minimal, and a high
358 proportion of light hydrocarbons is produced.

359 The cracking efficiency is easily seen on 2D COS maps (Figure 8A). The positive cross-peaks on 2D COS
360 maps, spreading from $1475\text{--}1425\text{ cm}^{-1}$ and $1383\text{--}1345\text{ cm}^{-1}$ are more intense on the X-Ray amorphous
361 EZ-ZSM-5 than on the other crystalline catalysts where cross-peaks are centered at 1461 and 1383
362 cm^{-1} . The positive correlation between the CH_3 and CH_2 deformation bands at *ca.* 1461 and 1383 cm^{-1}
363 evidence PP decomposition on the catalysts. A single band developing at 1383 cm^{-1} is associated with
364 the $\delta_s(CH_3)$ mode, whereas the peaks at 1360 and 1345 cm^{-1} witness the appearance of branched –
365 $CH(CH_3)_2$ and $-C(CH_3)_3$ terminations [48]. As the intensity of the CH_3 deformation bands is always higher
366 than CH_2 , the formation of the $CH_3(CH_2)_2CH_2^+$ species is proposed. This further supports the formation
367 of more branched products of partially cracked PP chains on EZ-ZSM-5, while on all other zeolites the
368 linear fragments dominate. Summing up, embryonic zeolites are more active in PO cracking as the
369 higher accessibility of their acid sites more than compensates their lower concentration and strength.
370 Higher bimolecular reaction rate in their supermicropores provides a distinct selectivity to branched

371 hydrocarbons. Contrarily, in desilicated zeolites transition states are not confined and stabilized by van
372 der Waals interactions in mesopores and display lower rates in acid-catalyzed PO cracking reactions.

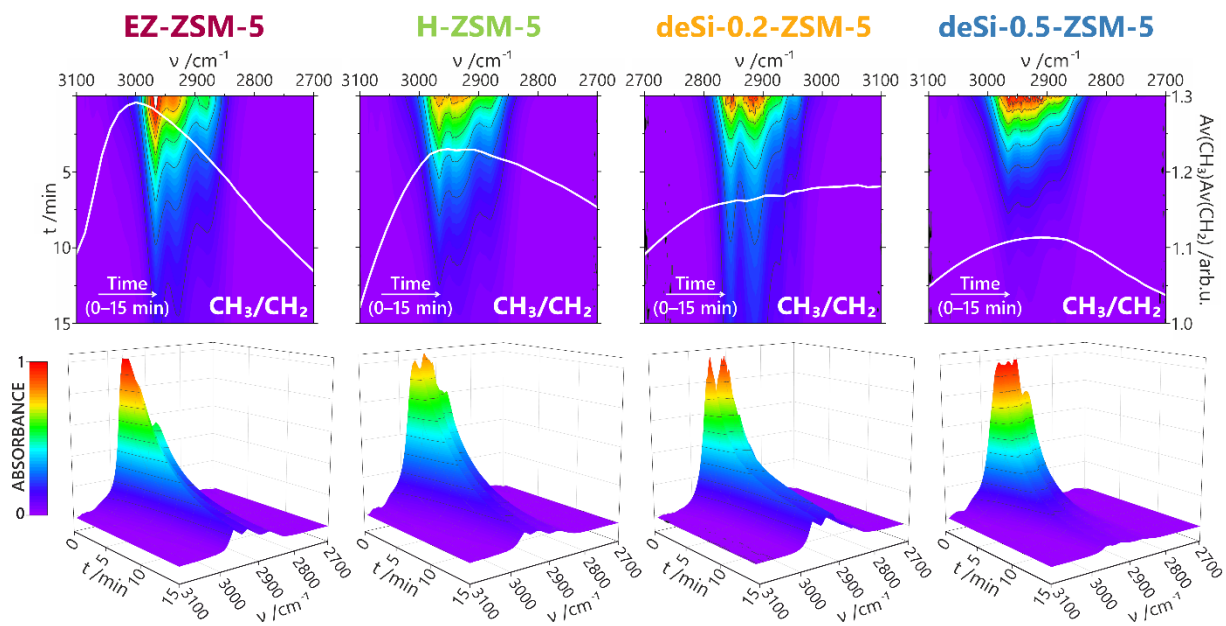
373 The accumulation of coke precursors on 2D COS maps (Fig. 8A) appears as a negative correlation
374 between CH₃/-CH₂ deformation bands (1461/1383 cm⁻¹) and the complex C=C stretching band (1620 -
375 1580 cm⁻¹). A sequence of catalytic events can be derived from a mutual analysis of synchronous (Fig.
376 8A) and asynchronous maps (Fig. 8B). The product of asynchronous and synchronous sets is one of the
377 straightforward insight into the interplay between the cracking and coking processes (Fig. 8C). The
378 analysis of the product maps is still based on the principles given by Noda [49]. In EZ-ZSM-5 the first
379 coke precursor is identified by the $\nu_{(C=C)ring}$ band at 1544 cm⁻¹, typical of polyolefins and methyl-
380 substituted benzyl cations or polycyclic aromatics characterized by the band centered at 1600-1590
381 cm⁻¹ [43,44]. The differentiated intensity of the peaks in product maps related to the CH₃ and CH₂
382 deformation region, *i.e.*, 1470-1300 cm⁻¹, indicates that PP cracking mechanism is ruled by the acidic
383 and textural properties of the catalysts. The band near 1480-1430 cm⁻¹ is associated with an
384 asymmetric out-of-plane CH₃ deformation, while the ca. 1393-1356 cm⁻¹ represents a symmetric in-
385 phase CH₃ deformations. When two methyls are bound to one saturated carbon in isopropyl or gem-
386 dimethyl groups, two bands with nearly equal intensity appear at 1385 and 1368 cm⁻¹ [50]. The 1330
387 cm⁻¹ band belongs to a C—H bending mode (C₃CH). The most complex picture of CH₃ and CH₂
388 vibrations is representative of EZ-ZSM-5 and the absence of tertiary C—H bending mode indicates the
389 preservation of longer chains of PP on the EZ-ZSM-5 surface. From the sequential order of events, it
390 can be anticipated that the coke precursors formations (1620 - 1580 cm⁻¹) are continuously integrated
391 with polymer cracking on EZ-ZSM-5. In contrast, H-ZSM-5 and deSi-0.5-ZSM-5 with the same number
392 of Brønsted acid sites activate the cyclization and aromatization processes which precede the cracking
393 of PP; the dominant coke precursors bands are gathered in the 1650-1580 cm⁻¹ spectral region. In deSi-
394 0.2-ZSM-5, the ultimate processing of PP is coking of the catalyst, as identified by the formation of
395 trisubstituted aromatics and/or polycyclic aromatics to a significant extent (1625-1600 cm⁻¹). The
396 catalyst-coking susceptibility is discussed further later.

397

398

399

400

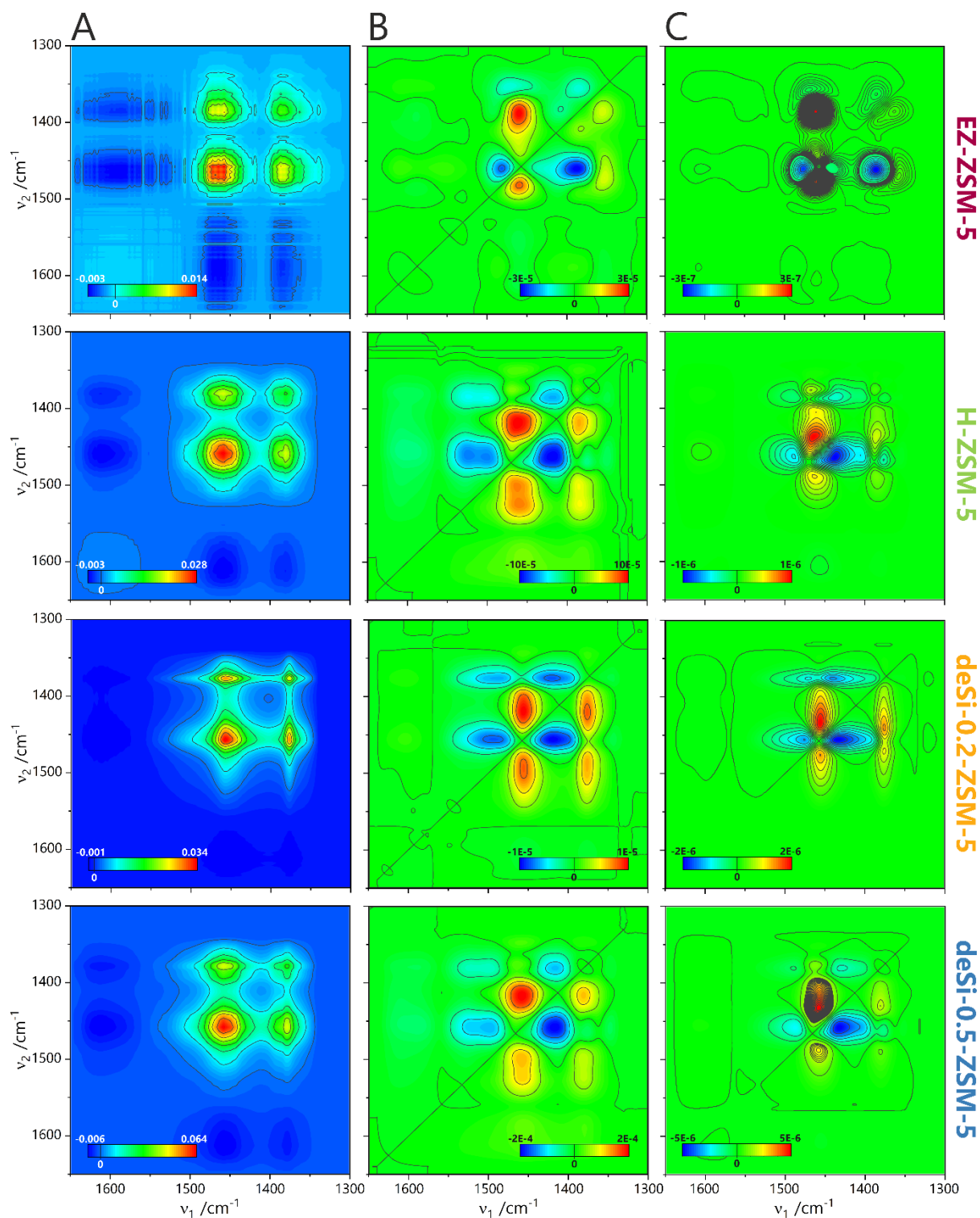


401

402 **Figure 7.** Top-projection of 3-D maps (bottom row) of the evolution of C–H stretching band intensity within 15
 403 min of PP cracking. The white curve (top row) represents changes in the CH₃/CH₂ bands area ratio.

404

405



406

407 **Figure 8.** 2D COS IR synchronous (A), asynchronous (B) maps and their product (C) illustrating coke formation
 408 during PP cracking. The colour coding (inset) represents correlation levels between the respective bands.

409

410

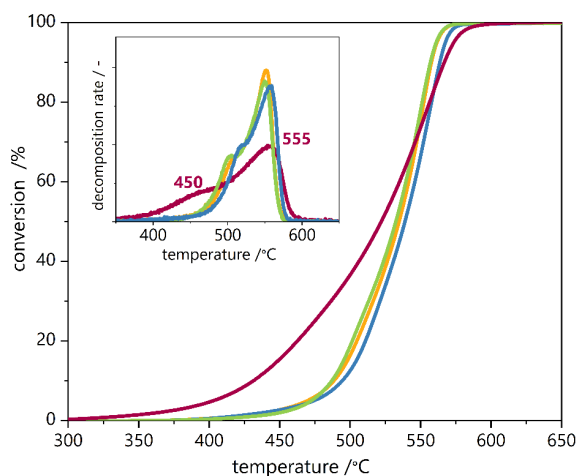
411

412 3.4 Coke burn-off: thermogravimetry and *operando* FT IR-TPO-MS

413 As coke deactivation of a catalyst changes its activity and selectivity, understanding the related
414 hydrogen transfer processes is important. An earlier scheme [51] describes successive oligomerization,
415 cyclization, and dehydrogenation of small molecules on active sites located in zeolite pores: alkanes -
416 alkenes - oligomers - naphthenes - aromatics - coke. The time evolution of the $Av(-CH_3)/Av(-CH_2)$ in
417 Fig. 7, indicates that hierarchical zeolites (deSi-0.5-ZSM-5 and deSi-0.2-ZSM-5) exhibit lower coke
418 formation and slower deactivation. This is due to an easier transport of reactants in the zeolites as well
419 as a lowering of diffusional restrictions on secondary products. The FT-IR 2D COS maps of the PP
420 cracking (Fig. 8) indicate a correlation between polymer chains cracking and the simultaneous
421 formation of unsaturated non-volatile high-carbon species identified by the cross peaks in the
422 $1650-1570\text{ cm}^{-1}$ region (maximum at ca. 1605 cm^{-1}). This implies that in H-ZSM-5 and deSi-ZSM-5
423 zeolites, coke consists of both methyl-substituted cycloalkenyl carbenium ions species, methyl-
424 substituted benzene cations or polycyclic aromatic compounds. Thus a high number of strong BAS
425 promotes condensations and aromatizations [43,52,53]. On EZ-ZSM-5, coke species are more diverse,
426 as in addition to the 1605 cm^{-1} species, bands in the $1565-1525\text{ cm}^{-1}$ region attest the presence of
427 alkyl aromatics (alkylbenzenes) and conjugated olefinic species $(C_nH_{2n+1})^+$ [54,55]. The microporous
428 structure of EZ-ZSM-5 reduces the heavy coke fractions.

429 Coke combustion under air is a common procedure to evaluate its nature and of course to regenerate
430 an industrial catalyst. The amount of coke estimated from TGA is higher on EZ-ZSM-5 (5.5%) than on
431 H-ZSM-5 (1.4%), and the hierarchical deSi-0.2-ZSM-5 (2.1%) and deSi-0.5-ZSM-5 (1.15%). It is related
432 to the coking rates observed on the time evolution of the $Av(-CH_3)/Av(-CH_2)$ ratio (Fig. 7), where EZ-
433 ZSM-5 is the highest. Coke oxidation starts on molecules located on the catalyst external surface and
434 then progresses inside the micropores, where oxygen availability becomes key. So, coke on EZ-ZSM-5
435 burns more rapidly than on H-ZSM-5 and deSi-ZSM-5. As the 2D COS IR analysis already showed that
436 coke species on EZ-ZSM-5 are more diverse, this accounts for the three steps ($450-555\text{ }^\circ\text{C}$) observed in
437 its light-off curve (Fig. 8). Magnoux and Guisnet [56] already concluded that both coking and coke
438 oxidation are shape-selective reactions. It is commonly agreed that in MFI-type zeolite, carbonaceous
439 compounds formed at channel intersections totally block oxygen diffusion during regeneration. On
440 large pore zeolites such as FAU and MOR, oxygen can still diffuse in their micropores. So, despite
441 extensive coking on EZ-ZSM-5, an efficient contact between reactants (coke and oxygen) facilitates
442 regeneration. In deSi-0.2-ZM-5, the denser coke located on its external surface is removed at higher
443 temperatures. The internal coke on deSi-0.2-ZSM-5 burns at still higher temperatures pointing to slow
444 oxygen diffusion in micropores blocked by carbonaceous residues at channel intersections. This result
445 confirms the high toxicity of coke on desilicated zeolites compared to embryonic ones. The high

446 micropore volume of EZ-ZSM-5 combined with a low Brønsted acidity prevents coke precursors to
447 evolve into heavy toxic coke as found on the crystalline zeolites.



448

449 **Figure 9.** Coke light-off curves and their derivatives (inset).

450

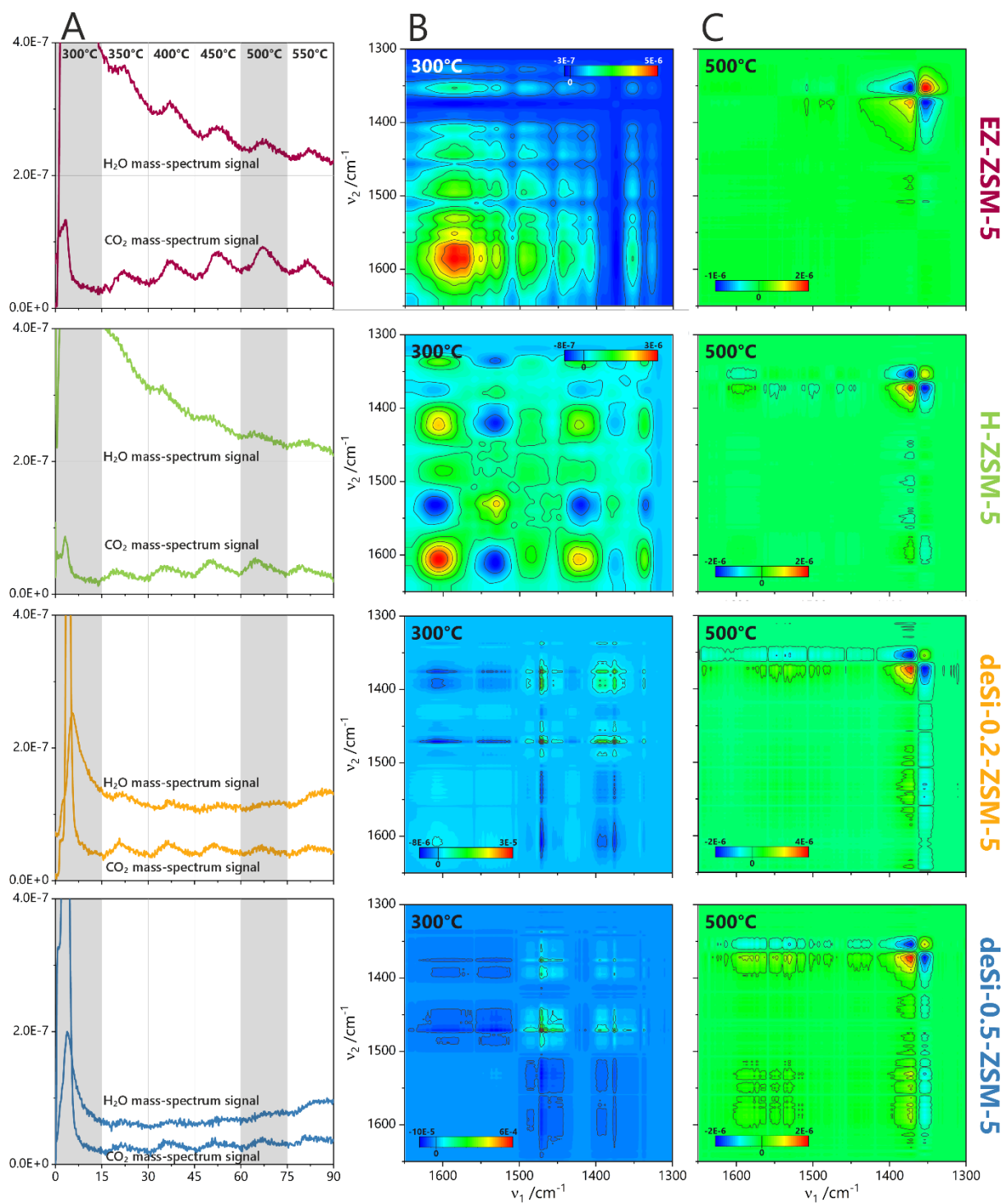
451 On deSi-0.2-ZSM-5, stronger retention of coke and its precursors is favored by the presence of stronger
452 acid sites. Carbenium ions adsorbed in zeolite micropores are stabilized by framework oxygens, acting
453 as weak bases conjugated with the strong acid sites. Such carbenium ions are less susceptible to
454 desorption as this requires a proton abstraction the carbenium ion, impossible on a weak base. The
455 long residence time of carbenium ions in deSi-0.2-ZSM-5 contributes to coke formation by
456 oligomerization, elimination, and ion-ion disproportionation. On deSi-0.5-ZSM-5, a lower Si/Al
457 produces framework oxygen of higher basicity, reducing the rate of bimolecular reactions between
458 adjacent ions by enhancing proton abstraction from the carbenium ion and hence a desorption of
459 olefins (*cf.* selectivities on Fig. 6). This effect is more significant than faster diffusion resulting from the
460 greater mesoporosity of deSi-0.5-ZSM-5. In the case of EZ-ZSM-5 more coking and significantly higher
461 production of *iso*-C₄ and *iso*-C₅ paraffins indicate faster hydrogen, not due to a higher BAS strength but
462 by the more open voids in EZ-ZSM-5, akin to those found in extra-large microporous materials. This
463 nature of coke in EZ-ZSM-5 is detailed in their TGA profiles, and IR explains its removal by combustion.

464 Silanols also impact catalyst deactivation, as observed on EZ-ZSM-5 and deSi-0.2-ZSM-5, the two
465 materials with the highest population. The highest level of coke observed is on EZ-ZSM-5 where
466 internal silanols are predominant, while on deSi-0.2-ZSM-5 with external silanols, coke and
467 deactivation are lower. It highlights further that different types of silanols have a direct influence on
468 coke formation and its preferential location on the most acidic silanols, as observed elsewhere [37].
469 While in mildly hierarchical deSi-0.2-ZSM-5 coking is driven by strong BAS located in the native

470 microporosity, in X-ray amorphous EZ-ZSM-5, acidic internal silanols and a higher microporosity
471 promote a higher degree of coking.

472 Further information on the coke nature is provided during an *operando* IR-TPO-MS monitoring of coke
473 removal (Fig. 10). CO₂ and H₂O formed during the temperature-programmed oxidation (TPO, 5% of O₂
474 in N₂) of carbonaceous species are monitored by mass spectrometry. TPO is performed at 300, 350,
475 400, 450, 500, and 550 °C; at each temperature, a 10 min isotherm step is maintained before increasing
476 the temperature further at a rate of 10 °C/min. Only the corresponding 2D COS IR maps highlighting
477 changes in spectral features during regeneration at 300 °C and 500 °C are discussed further (Figure 10).
478 In the case of catalysts with high microporosity, H-ZSM-5 and EZ-ZSM-5, H₂O (m/z = 18) production is
479 maintained throughout the process and greatly exceeds CO₂ production. On the hierarchical zeolites,
480 deSi-0.2-ZSM-5 and deSi-0.5-ZSM-5, less H₂O is produced at a slightly higher level than CO₂. The high
481 level of water production in the first stages of the TPO is associated with the burning of unreacted PP
482 (conversion under isothermal *operando* conditions at 250 °C does not reach 100%). This is illustrated
483 on 2D COS IR maps of coke combustion at 300 °C. The observed correlations between the C=C
484 stretching modes (1605 cm⁻¹) and asymmetric (1425 cm⁻¹) or symmetric modes of alkyl groups (1340
485 cm⁻¹) in aliphatics and alkyl aromatics indicates the presence of hydrocarbons with high H/C on the
486 external surface of H-ZSM-5 and EZ-ZSM-5. For deSi-0.5-ZSM-5 and deSi-0.2-ZSM-5, with added
487 intracrystalline mesoporosity, a much lower H₂O/CO₂ ratio is observed during the entire TPO,
488 indicating coke with lower H/C is combusted. The 2D COS IR maps of desi-0.5-ZSM-5 and desi-0.2-ZSM-
489 5 do not show any significant correlation between C=C and alkyl vibration during combustion at 300
490 °C. The CO₂ and H₂O production in the final stages of coke combustion is constant on all the catalysts,
491 albeit significantly higher for EZ-ZSM-5 and H-ZSM-5. This also appears in the 2D COS IR maps during
492 coke oxidation at 500 °C (Fig. 10). The patterns in the synchronous spectrum of the CH₃ and CH₂
493 deformation modes (1380–1340 cm⁻¹) are referred to as “angel” patterns with cross peak wings. They
494 appear when bands shift to higher frequencies together with some intensity increase, usually the result
495 of recording spectra at increasing temperatures. In our case, since temperature remains constant,
496 temperature-induced shift of the CH₃ band can be excluded. Such angel patterns are thus not artifacts
497 but reflect complex spectral changes in position and line shape of IR bands related to coke species. All
498 changes are, therefore, due to the interaction of oxygen with the carbonaceous species. The angel
499 pattern involves terminal CH₃ symmetric mode (1383 cm⁻¹) and branched –CH(CH₃)₂ and –C(CH₃)₃
500 terminations (1360 and 1345 cm⁻¹, resp.). A longer contact time between the spent catalyst and oxygen
501 increases the conversion of –CH₃ from branched ramifications to terminal isolated methyl groups.
502 Independently from the catalyst, coke oxidation is therefore initiated on methyl groups forming
503 oxygenated intermediates further decomposed into CO₂.

504 Correlation peaks are observed between polyaromatics (the C=C stretching modes at 1605 cm^{-1}) and
505 methyl groups ($1400\text{--}1325\text{ cm}^{-1}$) in H-ZSM-5 and hierarchical materials, while no such correlation
506 appear in the with EZ-ZSM-5; only very weak correlations between aliphatics and conjugated olefins
507 ($1525\text{--}1480\text{ cm}^{-1}$) appear. While in H-ZSM-5 and mesoporous deSi-0.2-ZSM-5 and deSi-0.5-ZSM-5 coke
508 oxidation are initiated on the $-\text{CH}(\text{CH}_3)_2$ and $-\text{C}(\text{CH}_3)_3$ groups on aromatic rings, on EZ-ZSM-5 oxidation
509 starts on alkyl species, as the aliphatics decrease independently of the coke.
510
511



512

513 **Figure 10.** TPO of coked catalysts illustrated as the mass signal intensity of the CO₂ ($m/z = 44$) and H₂O ($m/z = 18$)
 514 evolved gases at increasing temperatures (A). 2D COS IR synchronous maps of correlated events during coke
 515 oxidation at 300 °C (B) and 500 °C (C). The colour coding represents the correlation between the respective bands
 516 (insets).

517

518

519 CONCLUSIONS

520 This study highlights the complexity of a model polyolefin (PO), pure polypropylene, cracking on
521 various forms of the H-ZSM-5 zeolite, namely an embryonic, a purely microporous, and hierarchical
522 ones. Two zeolite parameters play complementary roles, namely porosity, and acid site strength
523 related to confinement. Our paper shows that FCC type of catalysts are a good basis to design a PO
524 depolymerization process. Highly accessible acid sites in EZ-ZSM-5 are required to attack the bulky
525 polymer and protons confined in micropores take advantage to bimolecular reactions to fine-tune
526 selectivity towards final products. Therefore, we need to work with well-defined and controlled
527 catalysts to understand the mode of action of poorly described FCC catalysts (the patented
528 preparations are never mentioned in the open literature when commercial FCC catalysts are used to
529 crack PO).

530 The complexity is also a source of opportunities to design catalysts dedicated to the chemical recycling
531 of polyolefins in an FCC type of process. The rapid but reversible catalyst deactivation followed by its
532 regeneration makes PP chemical recycling to fuel or petrochemical possible in existing and already
533 optimized FCC units.

534 The overall methodology sheds light on the chemistry of the process, including catalyst regeneration.
535 The relative role of the microporous and mesoporous surfaces of zeolites are highlighted and the
536 *operando* FT-IR study can be used at two levels: 1) understanding the fundamentals of the intricate
537 catalyst reactants/products interactions during the reaction, and 2) fingerprinting the catalyst behavior
538 to better optimize its design. The evaluation of the processing of PO in FCC should not be limited to
539 MFI type zeolites, but others like FAU (used in current FCC catalysts), BEA... should be considered or
540 mixtures thereof. It is probable that if such catalytic PO recycling takes place in existing or grass-root
541 FCC units, many options exist to fine-tune the design of drop-in catalysts by combining the presence
542 of various zeolites or amorphous components, as already practiced in the processing of heavy and
543 highly polluted oil fractions [4]. As in the current FCC operations, the heat requirements of the
544 (endothermic) cracking can be met by the (exothermic) coke combustion with the catalyst
545 microspheres playing the role of the heat transfer fluid.

546

547 ACKNOWLEDGEMENTS

548 This research was funded in whole or in part by National Science Centre, Poland [the Grant No
549 2021/43/B/ST4/00307]. For the purpose of Open Access, the author has applied a CC-BY public
550 copyright licence to any Author Accepted Manuscript (AAM) version arising from this submission. The

551 study was carried out using research infrastructure purchased with the funds of the European Union
552 in the framework of the Smart Growth Operational Programme, Measure 4.2; Grant No.
553 POIR.04.02.00-00-D001/20, "ATOMIN 2.0 - ATOMIC scale science for the INnovative economy". The
554 open-access publication of this article has been supported by a grant from the Faculty of Chemistry
555 under the Strategic Programme Excellence Initiative at Jagiellonian University.

556 References

- 557 [1] T. Hundertmark, C. McNally, T.J. Simons, H. Vanthournout, No time to waste: What plastics recycling
558 could offer, *McKinsey Chem.* (2018).
559 [https://doi.org/https://www.mckinsey.com/industries/chemicals/our-insights/no-time-to-waste-what-](https://doi.org/https://www.mckinsey.com/industries/chemicals/our-insights/no-time-to-waste-what-plastics-recycling-could-offer)
560 [plastics-recycling-could-offer.](https://doi.org/https://www.mckinsey.com/industries/chemicals/our-insights/no-time-to-waste-what-plastics-recycling-could-offer)
- 561 [2] Y. Wang, Y. Zhang, H. Fan, P. Wu, M. Liu, X. Li, J. Yang, C. Liu, P. Bai, Z. Yan, Elucidating the structure-
562 performance relationship of typical commercial zeolites in catalytic cracking of low-density
563 polyethylene, *Catal. Today.* 405–406 (2022) 135–143. <https://doi.org/10.1016/J.CATTOD.2022.06.024>.
- 564 [3] Y.H. Seo, K.H. Lee, D.H. Shin, Investigation of catalytic degradation of high-density polyethylene by
565 hydrocarbon group type analysis, *J. Anal. Appl. Pyrolysis.* 70 (2003) 383–398.
566 [https://doi.org/10.1016/S0165-2370\(02\)00186-9](https://doi.org/10.1016/S0165-2370(02)00186-9).
- 567 [4] W. Vermeiren, J.-P. Gilson, Impact of Zeolites on the Petroleum and Petrochemical Industry, *Top. Catal.*
568 52 (2009) 1131–1161. <https://doi.org/10.1007/s11244-009-9271-8>.
- 569 [5] S. Mintova, J.-P. Gilson, V. Valtchev, Advances in nanosized zeolites, *Nanoscale.* 5 (2013) 6693–6703.
570 <https://doi.org/10.1039/C3NR01629C>.
- 571 [6] K.-G. Haw, J.-M. Goupil, J.-P. Gilson, N. Nesterenko, D. Minoux, J.-P. Dath, V. Valtchev, Embryonic ZSM-
572 5 zeolites: zeolitic materials with superior catalytic activity in 1,3,5-triisopropylbenzene dealkylation,
573 *New J. Chem.* 40 (2016) 4307–4313. <https://doi.org/10.1039/C5NJ03310A>.
- 574 [7] K.-G. Haw, J.-P. Gilson, N. Nesterenko, M. Akouche, H. El Siblani, J.-M. Goupil, B. Rigaud, D. Minoux, J.-
575 P. Dath, V. Valtchev, Supported Embryonic Zeolites and their Use to Process Bulky Molecules, *ACS*
576 *Catal.* 8 (2018) 8199–8212. <https://doi.org/10.1021/acscatal.8b01936>.
- 577 [8] M. Akouche, J.-P. Gilson, N. Nesterenko, S. Moldovan, D. Chateigner, H. El Siblani, D. Minoux, J.-P. Dath,
578 V. Valtchev, Synthesis of Embryonic Zeolites with Controlled Physicochemical Properties, *Chem. Mater.*
579 32 (2020) 2123–2132. <https://doi.org/10.1021/acs.chemmater.9b05258>.
- 580 [9] A. Palčić, S.N. Jaén, D. Wu, M. Cai, C. Liu, E.A. Pidko, A.Y. Khodakov, V. Ordonsky, V. Valtchev,
581 Embryonic zeolites for highly efficient synthesis of dimethyl ether from syngas, *Microporous*
582 *Mesoporous Mater.* 322 (2021) 111138. <https://doi.org/10.1016/J.MICROMESO.2021.111138>.
- 583 [10] D. Verboekend, S. Mitchell, M. Milina, J.C. Groen, J. Pérez-Ramírez, Full Compositional Flexibility in the
584 Preparation of Mesoporous MFI Zeolites by Desilication, *J. Phys. Chem. C.* 115 (2011) 14193–14203.
585 <https://doi.org/10.1021/jp201671s>.
- 586 [11] K. Sadowska, K. Góra-Marek, J. Datka, Hierarchic zeolites studied by IR spectroscopy: Acid properties of
587 zeolite ZSM-5 desilicated with NaOH and NaOH/tetrabutylamine hydroxide, *Vib. Spectrosc.* 63 (2012)
588 418–425. <https://doi.org/10.1016/J.VIBSPEC.2012.09.007>.
- 589 [12] K. Góra-Marek, K. Tarach, M. Choi, 2,6-Di-tert-butylpyridine Sorption Approach to Quantify the External
590 Acidity in Hierarchical Zeolites, *J. Phys. Chem. C.* 118 (2014) 12266–12274.
591 <https://doi.org/10.1021/jp501928k>.
- 592 [13] M. Thommes, K. Kaneko, A. V Neimark, J.P. Olivier, F. Rodriguez-Reinoso, J. Rouquerol, K.S.W. Sing,
593 Physisorption of gases, with special reference to the evaluation of surface area and pore size
594 distribution (IUPAC Technical Report), *Pure Appl. Chem.* 87 (2015) 1051–1069.

- 595 <https://doi.org/doi:10.1515/pac-2014-1117>.
- 596 [14] C. Schlumberger, M. Thommes, Characterization of Hierarchically Ordered Porous Materials by
597 Physisorption and Mercury Porosimetry—A Tutorial Review, *Adv. Mater. Interfaces*. 8 (2021) 2002181.
598 <https://doi.org/https://doi.org/10.1002/admi.202002181>.
- 599 [15] K.A. Tarach, K. Góra-Marek, J. Martinez-Triguero, I. Melián-Cabrera, Acidity and accessibility studies of
600 desilicated ZSM-5 zeolites in terms of their effectiveness as catalysts in acid-catalyzed cracking
601 processes, *Catal. Sci. Technol.* 7 (2017) 858–873. <https://doi.org/10.1039/C6CY02609E>.
- 602 [16] K. Góra-Marek, M. Derewiński, P. Sarv, J. Datka, IR and NMR studies of mesoporous alumina and
603 related aluminosilicates, *Catal. Today*. 101 (2005) 131–138.
604 <https://doi.org/10.1016/J.CATTOD.2005.01.010>.
- 605 [17] I.C. Medeiros-Costa, E. Dib, N. Nesterenko, J.-P. Dath, J.-P. Gilson, S. Mintova, Silanol defect engineering
606 and healing in zeolites: opportunities to fine-tune their properties and performances, *Chem. Soc. Rev.*
607 50 (2021) 11156–11179. <https://doi.org/10.1039/D1CS00395J>.
- 608 [18] L. Lakiss, C. Kouvatas, J.-P. Gilson, V. Valtchev, S. Mintova, C. Fernandez, R. Bedard, S. Abdo, J. Bricker,
609 Atomic-Insight into Zeolite Catalyst Forming—an Advanced NMR Study, *J. Phys. Chem. C*. 125 (2021)
610 20028–20034. <https://doi.org/10.1021/acs.jpcc.1c05501>.
- 611 [19] K.A. Tarach, K. Pyra, K. Góra-Marek, Opening up ZSM-5 Hierarchical Zeolite’s Porosity through
612 Sequential Treatments for Improved Low-Density Polyethylene Cracking, *Molecules*. 25 (2020).
613 <https://doi.org/10.3390/molecules25122878>.
- 614 [20] K. Khivantsev, N.R. Jaegers, L. Kovarik, M.A. Derewinski, J.-H. Kwak, J. Szanyi, On the Nature of Extra-
615 Framework Aluminum Species and Improved Catalytic Properties in Steamed Zeolites, *Molecules*. 27
616 (2022). <https://doi.org/10.3390/molecules27072352>.
- 617 [21] N.S. Nesterenko, F. Thibault-Starzyk, V. Montouillout, V. V Yushchenko, C. Fernandez, J.-P. Gilson, F.
618 Fajula, I.I. Ivanova, The use of the consecutive adsorption of pyridine bases and carbon monoxide in the
619 IR spectroscopic study of the accessibility of acid sites in microporous/mesoporous materials, *Kinet.*
620 *Catal.* 47 (2006) 40–48. <https://doi.org/10.1134/S0023158406010071>.
- 621 [22] K. Tarach, K. Góra-Marek, J. Tekla, K. Brylewska, J. Datka, K. Mlekodaj, W. Makowski, M.C. Igualada
622 López, J. Martínez Triguero, F. Rey, Catalytic cracking performance of alkaline-treated zeolite Beta in
623 the terms of acid sites properties and their accessibility, *J. Catal.* 312 (2014) 46–57.
624 <https://doi.org/10.1016/J.JCAT.2014.01.009>.
- 625 [23] M. Boronat, A. Corma, What is measured when measuring acidity in zeolites with probe molecules?,
626 *ACS Catal.* 9 (2019) 1539–1548. <https://doi.org/10.1021/acscatal.8b04317>.
- 627 [24] A. Primo, H. Garcia, Zeolites as catalysts in oil refining, *Chem. Soc. Rev.* 43 (2014) 7548–7561.
628 <https://doi.org/10.1039/C3CS60394F>.
- 629 [25] J. Dwyer, F.R. Fitch, E.E. Nkang, Dependence of zeolite properties on composition. Unifying concepts, *J.*
630 *Phys. Chem.* 87 (1983) 5402–5404. <https://doi.org/10.1021/j150644a019>.
- 631 [26] K. Góra-Marek, I. Melián-Cabrera, A note on the acid strength of porous materials assessed by thermal
632 methods, *Microporous Mesoporous Mater.* 310 (2021) 110638.
633 <https://doi.org/https://doi.org/10.1016/j.micromeso.2020.110638>.
- 634 [27] I.C. Medeiros-Costa, E. Dib, F. Dubray, S. Moldovan, J.-P. Gilson, J.-P. Dath, N. Nesterenko, H.A.
635 Aleksandrov, G.N. Vayssilov, S. Mintova, Unraveling the Effect of Silanol Defects on the Insertion of
636 Single-Site Mo in the MFI Zeolite Framework, *Inorg. Chem.* 61 (2022) 1418–1425.
637 <https://doi.org/10.1021/acs.inorgchem.1c03076>.
- 638 [28] A.B. Fernández, I. Lezcano-Gonzalez, M. Boronat, T. Blasco, A. Corma, NMR spectroscopy and
639 theoretical calculations demonstrate the nature and location of active sites for the Beckmann
640 rearrangement reaction in microporous materials, *J. Catal.* 249 (2007) 116–119.
641 <https://doi.org/10.1016/J.JCAT.2007.03.030>.

- 642 [29] L. Dalstein, E. Potapova, E. Tyrode, The elusive silica/water interface: isolated silanols under water as
643 revealed by vibrational sum frequency spectroscopy, *Phys. Chem. Chem. Phys.* 19 (2017) 10343–10349.
644 <https://doi.org/10.1039/C7CP01507K>.
- 645 [30] E. Dib, I.M. Costa, G.N. Vayssilov, H.A. Aleksandrov, S. Mintova, Complex H-bonded silanol network in
646 zeolites revealed by IR and NMR spectroscopy combined with DFT calculations, *J. Mater. Chem. A* 9
647 (2021) 27347–27352. <https://doi.org/10.1039/D1TA06908J>.
- 648 [31] D. Verboekend, J.C. Groen, J. Pérez-Ramírez, Interplay of Properties and Functions upon Introduction of
649 Mesoporosity in ITQ-4 Zeolite, *Adv. Funct. Mater.* 20 (2010) 1441–1450.
650 <https://doi.org/https://doi.org/10.1002/adfm.200902205>.
- 651 [32] K. Pyra, K.A. Tarach, E. Janiszewska, D. Majda, K. Góra-Marek, Evaluation of the Textural Parameters of
652 Zeolite Beta in LDPE Catalytic Degradation: Thermogravimetric Analysis Coupled with FTIR Operando
653 Studies, *Molecules*. 25 (2020). <https://doi.org/10.3390/molecules25040926>.
- 654 [33] K. Pyra, K.A. Tarach, D. Majda, K. Góra-Marek, Desilicated zeolite BEA for the catalytic cracking of LDPE:
655 the interplay between acidic sites' strength and accessibility, *Catal. Sci. Technol.* 9 (2019) 1794–1801.
656 <https://doi.org/10.1039/C9CY00326F>.
- 657 [34] G. Manos, A. Garforth, J. Dwyer, Catalytic Degradation of High-Density Polyethylene over Different
658 Zeolitic Structures, *Ind. Eng. Chem. Res.* 39 (2000) 1198–1202. <https://doi.org/10.1021/ie990512q>.
- 659 [35] Q. Zhou, L. Zheng, Y.Z. Wang, G.M. Zhao, B. Wang, Catalytic degradation of low-density polyethylene
660 and polypropylene using modified ZSM-5 zeolites, *Polym. Degrad. Stab.* 84 (2004) 493–497.
661 <https://doi.org/10.1016/J.POLYMDEGRADSTAB.2004.01.007>.
- 662 [36] K. Pyra, K.A. Tarach, K. Góra-Marek, Towards a greater olefin share in polypropylene cracking –
663 Amorphous mesoporous aluminosilicate competes with zeolites, *Appl. Catal. B Environ.* 297 (2021)
664 120408. <https://doi.org/10.1016/J.APCATB.2021.120408>.
- 665 [37] B. Reiprich, K.A. Tarach, K. Pyra, G. Grzybek, K. Góra-Marek, High-Silica Layer-like Zeolites Y from
666 Seeding-Free Synthesis and Their Catalytic Performance in Low-Density Polyethylene Cracking, *ACS*
667 *Appl. Mater. Interfaces*. 14 (2022) 6667–6679. <https://doi.org/10.1021/acsami.1c21471>.
- 668 [38] K.A. Cumming, B.W. Wojciechowski, Hydrogen Transfer, Coke Formation, and Catalyst Decay and Their
669 Role in the Chain Mechanism of Catalytic Cracking, *Catal. Rev.* 38 (1996) 101–157.
670 <https://doi.org/10.1080/01614949608006455>.
- 671 [39] S. Li, A. Zheng, Y. Su, H. Zhang, L. Chen, J. Yang, C. Ye, F. Deng, Brønsted/Lewis Acid Synergy in
672 Dealuminated HY Zeolite: A Combined Solid-State NMR and Theoretical Calculation Study, *J. Am.*
673 *Chem. Soc.* 129 (2007) 11161–11171. <https://doi.org/10.1021/ja072767y>.
- 674 [40] M. Derewiński, K. Góra-Marek, K. Lázár, J. Datka, Nature of active sites in the Fe-TON Zeolites:
675 Mössbauer and IR studies, *Stud. Surf. Sci. Catal.* 174 (2008) 865–868. [https://doi.org/10.1016/S0167-2991\(08\)80025-0](https://doi.org/10.1016/S0167-2991(08)80025-0).
- 677 [41] A. Corma, P.J. Miguel, A. V. Orchillés, The Role of Reaction Temperature and Cracking Catalyst
678 Characteristics in Determining the Relative Rates of Protolytic Cracking, Chain Propagation, and
679 Hydrogen Transfer, *J. Catal.* 145 (1994) 171–180. <https://doi.org/10.1006/JCAT.1994.1020>.
- 680 [42] J. Abbot, B.W. Wojciechowski, Catalytic reactions of branched paraffins on HY zeolite, *J. Catal.* 113
681 (1988) 353–366. [https://doi.org/10.1016/0021-9517\(88\)90264-3](https://doi.org/10.1016/0021-9517(88)90264-3).
- 682 [43] K. Gołąbek, K.A. Tarach, K. Góra-Marek, Standard and rapid scan infrared spectroscopic studies of o-
683 xylene transformations in terms of pore arrangement of 10-ring zeolites – 2D COS analysis, *Dalt. Trans.*
684 46 (2017) 9934–9950. <https://doi.org/10.1039/C7DT00644F>.
- 685 [44] K.A. Tarach, K. Gołąbek, M. Choi, K. Góra-Marek, Quantitative infrared spectroscopic studies and 2D
686 COS analysis of xylenes isomerization over hierarchical zeolites, *Catal. Today*. 283 (2017) 158–171.
687 <https://doi.org/10.1016/J.CATTOD.2016.02.035>.

- 688 [45] P. Painter, M. Starsinic, M. Coleman, DETERMINATION OF FUNCTIONAL GROUPS IN COAL BY FOURIER
689 TRANSFORM INTERFEROMETRY, in: J.R. FERRARO, L.J. BASILE (Eds.), *Fourier Transform Infrared Spectra*,
690 Academic Press, San Diego, 1985: pp. 169–241. <https://doi.org/https://doi.org/10.1016/B978-0-12-254104-9.50011-0>.
691
- 692 [46] D.P. Serrano, J. Aguado, J.M. Escola, J.M. Rodriguez, A. Peral, Catalytic properties in polyolefin cracking
693 of hierarchical nanocrystalline HZSM-5 samples prepared according to different strategies, *J. Catal.* 276
694 (2010) 152–160. <https://doi.org/https://doi.org/10.1016/j.jcat.2010.09.008>.
- 695 [47] K.A. Tarach, K. Pyra, S. Siles, I. Melián-Cabrera, K. Góra-Marek, Operando Study Reveals the Superior
696 Cracking Activity and Stability of Hierarchical ZSM-5 Catalyst for the Cracking of Low-Density
697 Polyethylene, *ChemSusChem.* 12 (2019) 633–638. <https://doi.org/10.1002/cssc.201802190>.
- 698 [48] C. Lamberti, E. Groppo, G. Spoto, S. Bordiga, A. Zecchina, Infrared Spectroscopy of Transient Surface
699 Species, *Adv. Catal.* 51 (2007) 1–74. [https://doi.org/10.1016/S0360-0564\(06\)51001-6](https://doi.org/10.1016/S0360-0564(06)51001-6).
- 700 [49] I. Noda, Y. Ozaki, *Two-Dimensional Correlation Spectroscopy: Applications in Vibrational and Optical*
701 *Spectroscopy*, Wiley, 2004. <https://doi.org/10.1002/0470012404>.
- 702 [50] N.B. Colthup, L.H. Daly, S.E. Wiberley, CHAPTER 3 - MOLECULAR SYMMETRY, in: N.B. Colthup, L.H. Daly,
703 S.E. Wiberley (Eds.), *Intro. to Infrared Raman Spectrosc. (Second Ed., Second Ed)*, Academic Press,
704 1975: pp. 119–178. <https://doi.org/https://doi.org/10.1016/B978-0-12-182552-2.50006-1>.
- 705 [51] E.G. Derouane, Factors Affecting The Deactivation Of Zeolites By Coking, *Stud. Surf. Sci. Catal.* 20 (1985)
706 221–240. [https://doi.org/10.1016/S0167-2991\(09\)60173-7](https://doi.org/10.1016/S0167-2991(09)60173-7).
- 707 [52] J.F. Haw, J.B. Nicholas, W. Song, F. Deng, Z. Wang, T. Xu, C.S. Heneghan, Roles for Cyclopentenyl Cations
708 in the Synthesis of Hydrocarbons from Methanol on Zeolite Catalyst HZSM-5, *J. Am. Chem. Soc.* 122
709 (2000) 4763–4775. <https://doi.org/10.1021/ja994103x>.
- 710 [53] K. Gołębek, K.A. Tarach, K. Góra-Marek, 2D COS analysis of m-xylene transformation over medium-pore
711 zeolites, *Microporous Mesoporous Mater.* 266 (2018) 90–101.
712 <https://doi.org/10.1016/J.MICROMESO.2018.02.028>.
- 713 [54] Y. Ganjkhanelou, E. Groppo, S. Bordiga, M.A. Volkova, G. Berlier, Incorporation of Ni into HZSM-5
714 zeolites: Effects of zeolite morphology and incorporation procedure, *Microporous Mesoporous Mater.*
715 229 (2016) 76–82. <https://doi.org/10.1016/J.MICROMESO.2016.04.002>.
- 716 [55] K. Pyra, K.A. Tarach, A. Śrębowata, I. Melián-Cabrera, K. Góra-Marek, Pd-modified beta zeolite for
717 modulated hydro-cracking of low-density polyethylene into a paraffinic-rich hydrocarbon fuel, *Appl.*
718 *Catal. B Environ.* 277 (2020) 119070. <https://doi.org/10.1016/J.APCATB.2020.119070>.
- 719 [56] P. Magnoux, C. Canaff, F. Machado, M. Guisnet, Coking, aging, and regeneration of zeolites XIII.
720 Composition of the carbonaceous compounds responsible for the deactivation of a USHY zeolite during
721 toluene disproportionation, *J. Catal.* 134 (1992) 286–298. [https://doi.org/10.1016/0021-9517\(92\)90228-A](https://doi.org/10.1016/0021-9517(92)90228-A).
722

723